ELSEVIER

Volume 184, Issue 7, JULY 2011

JOURNAL OF SOLID STATE CHEMISTRY

www.elsevier.com/locate/jssc

CONTENTS

Abstracted/indexed in BioEngineering Abstracts, Chemical Abstracts, Coal Abstracts, Current Contents/Physics, Chemical, & Earth Sciences, Engineering Index, Research Alert, SCISEARCH, Science Abstracts, and Science Citation Index. Also covered in the abstract and citation database SCOPUS®. Full text available on ScienceDirect®.

Regular Articles

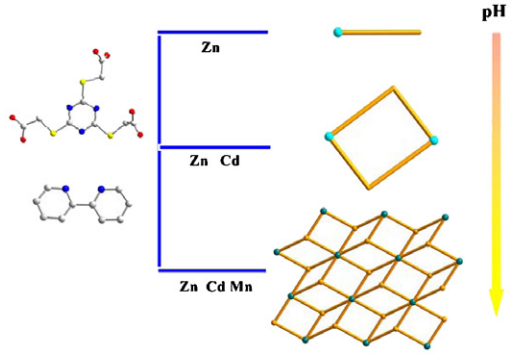

Six complexes based on a flexible tricarboxylate ligand exhibit rich structural chemistry from mononuclear to 2D (3,6)-connected networks. PH and metal ions have large influences on the resulting structures.

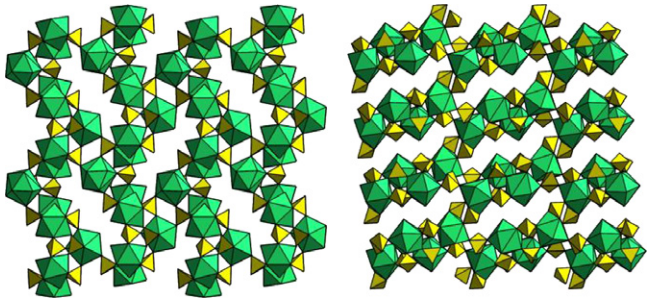

The structures of four hydrous thorium sulfates are reported that have structural units consisting of finite clusters, chains, and frameworks.

Regular Articles—Continued

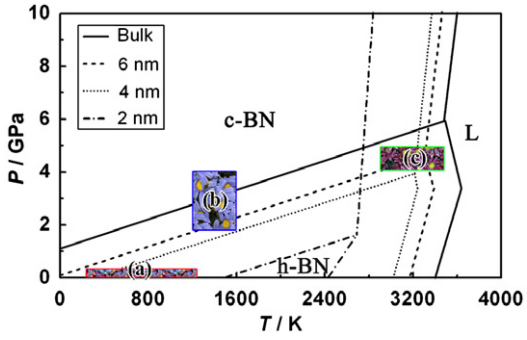

The size-dependent phase diagram of BN was developed on the basis of nanothermodynamic theory and it can be used to predict whether cubic BN (c-BN) can be formed at a given condition.

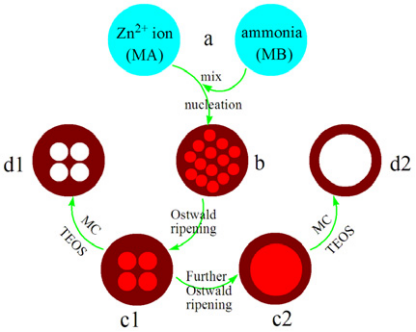

Formation process of SiO_2 nanospheres with porous and single hollow interior.

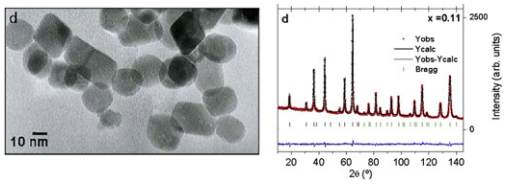

$ZnFe_2O_4$ nanoparticles of 19 nm obtained by the solvotermal method together with its Rietveld refined pattern.

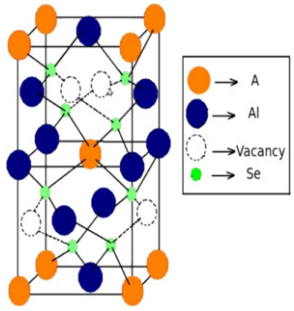

Band structure and TDOS show the band gaps and effect of structural distortion on electronic properties. PDOS shows effect of *p–d* hybridization on band gaps for all four compounds.

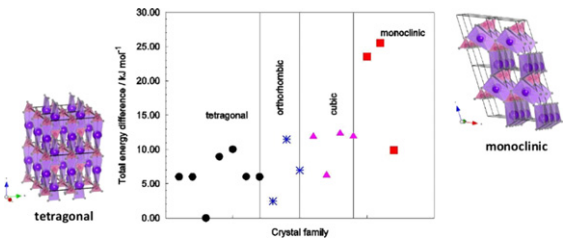

The total electron energy difference of the calculated stable structures. Here, the tetragonal (IT 137) and the monoclinic (IT 6) symmetry groups corresponded to the lowest and the highest energy structures, respectively.

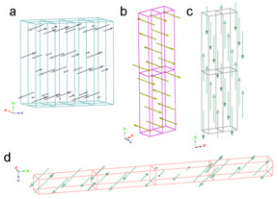

The magnetic structures of $RSn_{1+x}Ge_{1-x}$ (R = Tb, Dy, Ho and Er, $x \approx 0.1$) compounds have been determined by neutron diffraction studies on polycrystalline samples. The magnetic ordering in $TbSn_{1.12}Ge_{0.88}$ (a) is sine-modulated described by the propagation vector $\mathbf{k} = (0.426, 0, 0.588)$. The magnetic structures of $RSn_{1+x}Ge_{1-x}$ where R are Dy (b), Ho (b) and Er (c) at temperatures close to 1.5 K are described by the propagation vector $\mathbf{k} = (1/2, 1/2, 0)$ with the sequence $(+ + - +)$ of magnetic moments in the crystal unit cell. For Ho- and Dy-compound this ordering is stable up to T_N while for Er-compound at $T_t = 3.5$ K it tunes into a modulated structure (d).

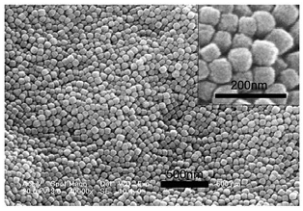

The uniform and monodisperse Cu_2O nanocube/polycarbazole composites were prepared by an one-pot solvothermal process. As covered by polycarbazole, the photocatalytic activities of Cu_2O nanocubes were improved. The polycarbazole not only protected and stabilized Cu_2O cubes, but also prohibited the recombination of photogenerated electrons–holes pair and facilitated interfacial charge transfer between polycarbazole and Cu_2O.

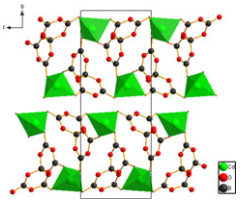

A new phase, $K_3CdB_5O_{10}$, has been discovered in the ternary K_2O–CdO–B_2O_3 system. The crystal structure consists of a two-dimensional infinite $[CdB_5O_{10}]$ layer.

Continued

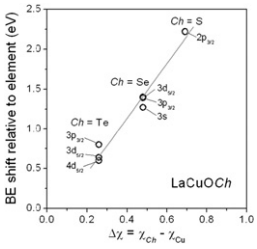

The presence of anionic chalcogen atoms in LaCuO*Ch* is supported by the *Ch* binding energies, which undergo negative shifts proportional to the polarity of the Cu–*Ch* bonds.

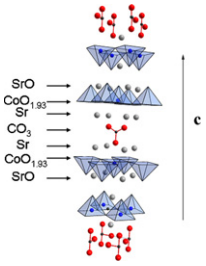

Structural model of the $Sr_4Co_2(CO_3)O_{5.86}$ oxycarbonate.

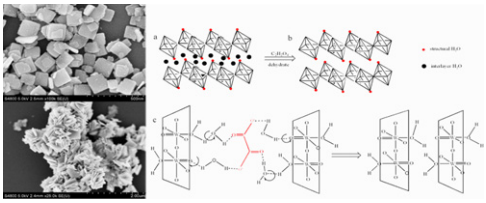

The oxalic acid has a key role for the structure of $WO_3 \cdot H_2O$ evolution from plates to flowers and the dehydration process of $WO_3 \cdot 2H_2O$ to $WO_3 \cdot H_2O$.

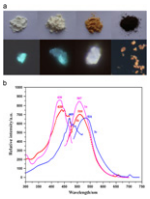

A green–blue luminescence occurs with an emission maximum at 507 nm upon excitation at 430 nm. The photoluminescence of **1a** can be modified from green–blue to white by means of a simple heat-treatment process.

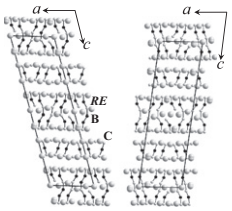

New ternary rare-earth metal boride carbides $RE_{25}B_{14}C_{26}$ (RE = Pr, Nd) and $Nd_{25}B_{12}C_{28}$ were synthesized by co-melting the elements. $Nd_{25}B_{12}C_{28}$ is stable up to 1440 K. $RE_{25}B_{14}C_{26}$ (RE = Pr, Nd) exist above 1270 K. The crystal structures were investigated by means of single-crystal X-ray diffraction. Their structures consist of a three-dimensional framework of rare-earth metal atoms resulting from the stacking of slightly corrugated and distorted square nets, leading to cavities filled with cumulene-like molecules $[B_2C_4]^{6-}$ and $[B_3C_3]^{7-}$, nearly linear $[BC_2]^{5-}$ and bent $[BC_2]^{7-}$ units and isolated carbon atoms, respectively. Structural and theoretical analysis suggests the ionic formulation for $RE_{25}B_{14}C_{26}$: $(RE^{3+})_{25}[B_2C_4]^{6-}([B_3C_3]^{7-})_2([BC_2]^{5-})_4([BC_2]^{7-})_2(C^{4-})_4 \cdot 5e^-$ and for $Nd_{25}B_{12}C_{28}$: $(Nd^{3+})_{25}([B_2C_4]^{6-})_3([BC_2]^{5-})_4([BC_2]^{7-})_2(C^{4-})_4 \cdot 7e^-$.

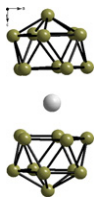

New transition elements doped $YB_{44}Si_2$ were synthesized and have nominal compositions $YB_{41.1}Si_{1.1}Rh_{0.02}$ and $YB_{41}Si_{1.3}Ni_{0.06}$. Insertion of transition elements into the crystal structure of $YB_{44}Si_2$ leads to the transformation of B_{12} icosahedra into B_{11} polyhedrons for a few percent of them.

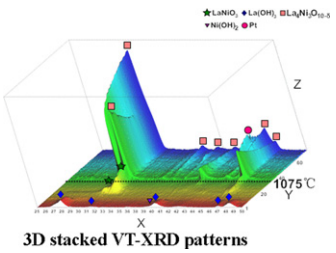

3D stacked VT-XRD patterns

In situ variable temperature XRD showing the phase formation pathway of $La_{n+1}Ni_nO_{3n+1}$ at evaluated temperatures.

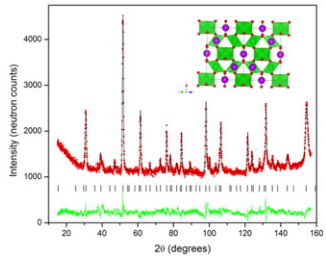

$Gd_2Zr_2O_7$ enriched in ^{160}Gd prepared. Neutron diffraction reveals ordering of the anions. Precise structure established.

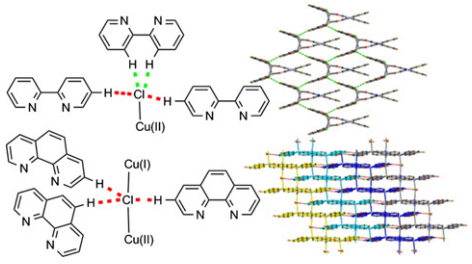

Subtly different C–H···Cl bonding nature leads to diverse coordination modes and supramolecular networks, as well as physical properties of two Cu^ICu^{II} coordination polymers with similar compositions.

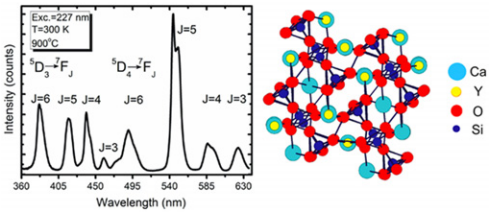

Luminescence of $Ca_3Y_2(Si_3O_9)_2$:Tb covers the whole visible region of electromagnetic spectrum and the relative intensity of the blue part against the green one depends on the activator content and technological parameters of preparation.

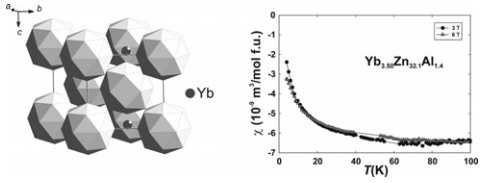

Crystal structure and magnetic susceptibility of $Yb_{3.50}Zn_{32.1}Al_{1.4}$.

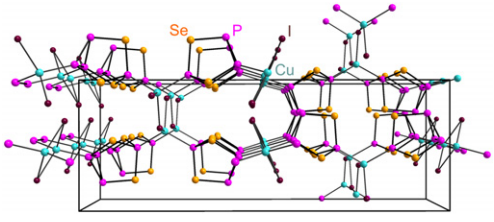

New coordination polymers have been prepared and characterized by the reaction of P_4Se_3 and copper(I) halides solutions under diffusion conditions.

Continued

Different geometrical arrangements in carboxylate coordination polymers of flexible dicarboxylic acid
Himangshu Deka, Rupam Sarma, Satchi Kumari, Alika Khare and Jubaraj B. Baruah
page 1726

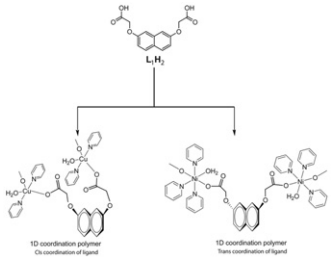

Different geometrical arrangements in coordination polymers derived from (7-carboxymethoxy-naphthalen-2-yloxy)-acetic acid of metal ions Mn(II), Ni(II), Cu(II), Zn(II) and Cd(II) are presented. The (5-carboxymethoxy-naphthalen-1-yloxy)-acetic acid led to hexa-aquo cadmium(II) dicarboxylate.

Growth of single crystalline dendritic Li_2SiO_3 arrays from $LiNO_3$ and mesoporous SiO_2
José M. Córdoba, Mohamed A. Ballem, Emma M. Johansson and Magnus Odén
page 1735

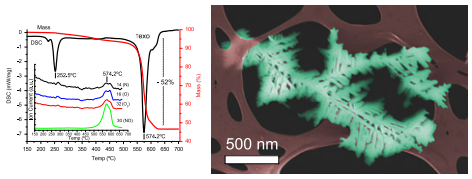

TG/DSC and gas analysis (inset) curves of the synthesis reaction measured in air and SEM micrograph of the Li_2SiO_3 dendrite obtained.

Rare configuration of tautomeric benzimidazolecarboxylate ligands in cadmium(II) and copper(II) coordination polymers
Jing-Yun Wu, Ciao-Wei Yang, Hui-Fang Chen, Yu-Chen Jao, Sheng-Ming Huang, Chiitang Tsai, Tien-Wen Tseng, Gene-Hsiang Lee, Shie-Ming Peng and Kuang-Lieh Lu
page 1740

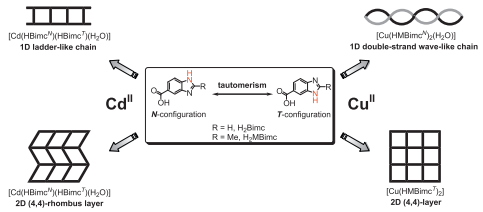

A pair of tautomeric HBimc building blocks (normal (*N*) and tautomer (*T*)) is found simultaneously in two Cd(II) networks, whereas, the normal and tautomer modes of HMBimc are present as separate entities in two Cu(II) frameworks. The isolation of a Cu(II) network with only a tautomer (*T*) mode of the benzimidazolecarboxylate-based ligand is achieved for the first time.

Fabrication of carbon microcapsules containing silicon nanoparticles–carbon nanotubes nanocomposite by sol–gel method for anode in lithium ion battery
Joonwon Bae
page 1749

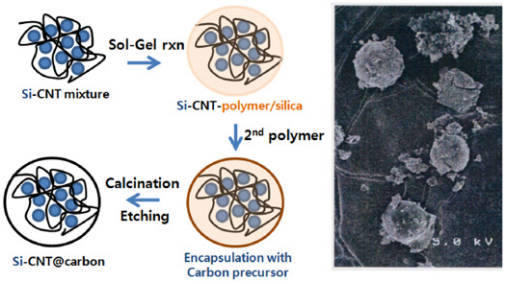

Carbon microcapsules containing silicon nanoparticles (Si NPs)–carbon nanotubes (CNTs) nanocomposite (Si-CNT@C) have been fabricated by a surfactant mediated sol–gel method.

New organically templated photoluminescence iodocuprates(I)
Qin Hou, Jin-Jing Zhao, Tian-Qi Zhao, Juan Jin, Jie-Hui Yu and Ji-Qing Xu
page 1756

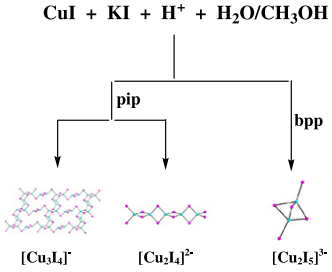

The solvothermal self-assemblies of CuI, KI and pip/bpp in acidic CH_3OH solutions created three iodocuprates 2-D layered [(Hpip)-Cu_3I_4] **1**, 1-D chained [tmpip][Cu_2I_4] **2** and dinuclear [H_2bpp]$_2$ [Cu_2I_5] $I \cdot 2H_2O$ **3**.

Modified SBA-15 as the carrier for metoprolol and papaverine: Adsorption and release study
Michał Moritz and Marek Łaniecki
page 1761

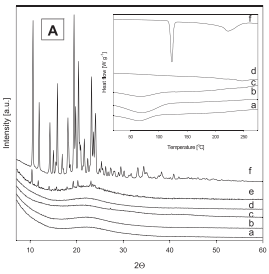

XRD and DSC of the –SO_3H modified SBA-15 loaded with metoprolol.

Microstructural features and domain formation in $(Ba,Sr)_2TiSi_2O_8$ fresnoites
Chui Ling Wong, Cristiano Ferraris and T.J. White
page 1768

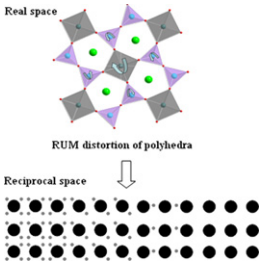

Fresnoite layers contain SiO_4 and TiO_5 polyhedra that undergo run rotation and tilting to create 3D, 4D and 5D structural modulations that can be directly observed by electron diffraction and high resolution imaging.

Syntheses and characterization of energetic compounds constructed from alkaline earth metal cations (Sr and Ba) and 1,2-bis(tetrazol-5-yl)ethane
Zhengqiang Xia, Sanping Chen, Qing Wei and Chengfang Qiao
page 1777

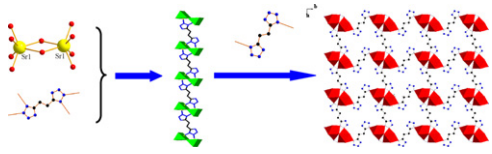

Two novel 2D isomorphous alkaline earth metal complexes were assembled by 4-connected $Sr_2(H_2O)_{10}/Ba_2(H_2O)_{10}$ SBUs and two independent binding modes of H_2BTE ligands, and the catalytic performances toward thermal decomposition of ammonium perchlorate and photoluminescent properties of them were investigated.

First-principle investigation of Jahn–Teller distortion and topological analysis of chemical bonds in $LiNiO_2$
Zhenlian Chen, Huamin Zou, Xiaopeng Zhu, Jie Zou and Jiefeng Cao
page 1784

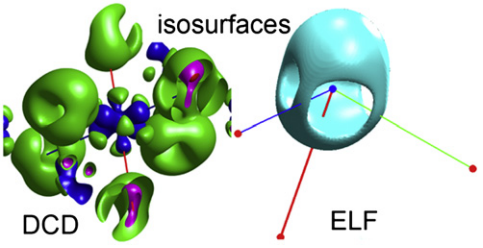

Isosurfaces of the difference charge density and the electron localization function for the zigzag structure of $LiNiO_2$.

The synthesis and complex anion-vacancy ordered structure of $La_{0.33}Sr_{0.67}MnO_{2.42}$
Edward Dixon, Joke Hadermann and Michael A. Hayward
page 1791

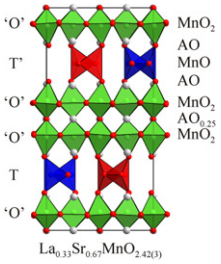

The topotactic reduction of the perovskite phase $La_{0.33}Sr_{0.67}MnO_3$ with NaH yields $La_{0.33}Sr_{0.67}MnO_{2.42(3)}$, which adopts a novel anion vacancy ordered structure with a 6-layer OOTOOT' stacking sequence of the 'octahedral' and tetrahedral layers. The anion site that links the neighbouring octahedral layers is partially occupied so only 25% of the 'octahedral' manganese sites actually have 6-fold MnO_6 coordination.

Hydrothermal synthesis of $[C_6H_{16}N_2][In_2Se_3(Se_2)]$: A new one-dimensional indium selenide
Sarah J. Ewing, Anthony V. Powell and Paz Vaqueiro
page 1800

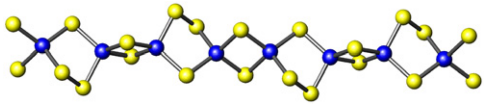

$[C_6H_{16}N_2][In_2Se_3(Se_2)]$, prepared under hydrothermal conditions, contains one-dimensional chains of stoichiometry $[In_2Se_3(Se_2)]^{2-}$, in which four-membered $[In_2Se_2]$ and five-membered $[In_2Se_3]$ rings alternate.

Highly ordered Zn-doped mesoporous silica: An efficient catalyst for transesterification reaction
Nabanita Pal, Manidipa Paul and Asim Bhaumik
page 1805

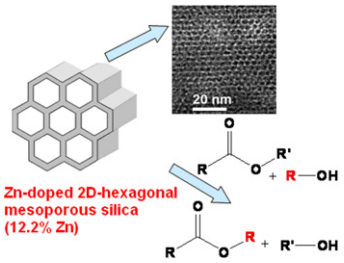

Zn-rich 2D-hexagonal mesoporous materials are synthesized hydrothermally, which show very good catalytic activity in the transesterification reaction under mild liquid phase reaction conditions.

Continued

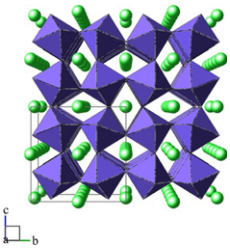

The CuO_x–TiO_2–Nb_2O_5 phase diagram was determined at 935 °C and contains one new phase, $Cu_{3.21}Ti_{1.16}Nb_{2.63}O_{12}$, pictured, a modest semiconductor with $\varepsilon_r \sim 63$, and one rutile-structured solid solution series, $Ti_{1-3x}Cu_xNb_{2x}O_2$.

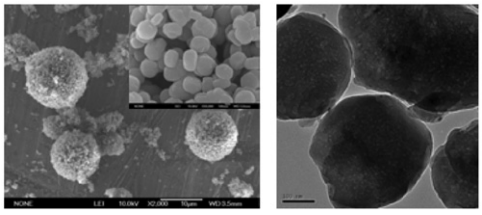

Mesoporous zeolite single crystals were synthesized by using cheap porogens as template.

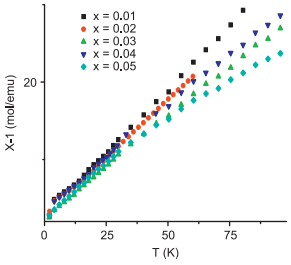

The least square fit to the modified Curie–Weiss law shows paramagnetic interaction in $Yb_{2-x}Cr_xO_3$ $(0 < x \leq 0.03)$. The $YbCrO_3$ phase impurity will have no influence on the magnetic properties of the samples with $x > 0.03$

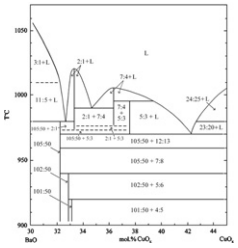

A diagram of phase relations in the BaO–CuO_x system in the range of 30.0–45.0 mol% CuO at 900–1050 °C at $P(O_2) = 21$ kPa (air) constructed on the data obtained by visual polythermal analysis (the liquidus line), XRD and ED with elemental analysis.

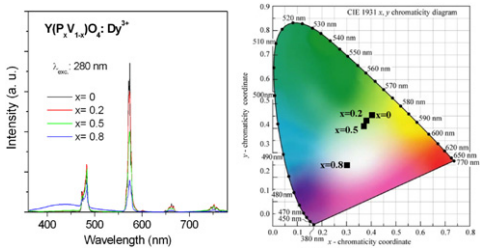

The relative intensities of the emission features and the color of the luminescence vary with the host composition along the $Y(P_xV_{1-x})O_4$:Dy^{3+} system.

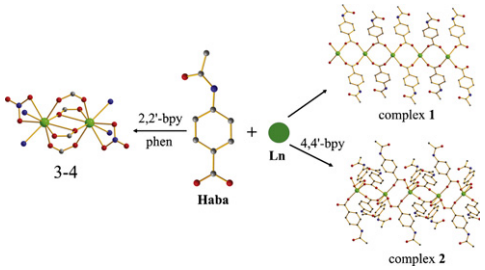

Structure variation of four complexes is attributed to the change of coligands and various coordination modes of aba molecules. Moreover, they show characteristic emissions in the visible region.

Chloride substitution in sodium borohydride
Dorthe B. Ravnsbæk, Line H. Rude and Torben R. Jensen
page 1858

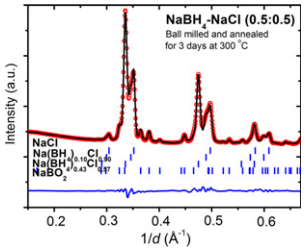

Dissolution of sodium chloride and sodium borohydride into each other resulting in formation of solid solutions of composition $Na(BH_4)_{1-x}Cl_x$ is studied. Dissolution is facilitated by two methods: ball milling or annealing at 300 °C for three days of $NaBH_4$–NaCl samples. Sample compositions and dissolution mechanism are studied by Rietveld refinement of synchrotron radiation powder X-ray diffraction data.

Titania–lanthanum phosphate photoactive and hydrophobic new generation catalyst
Chembolli K. Jyothi, Kanakkanmavudi B. Jaimy, Swapankumar Ghosh, Sasidharan Sankar, V.S. Smitha and K.G.K. Warrier
page 1867

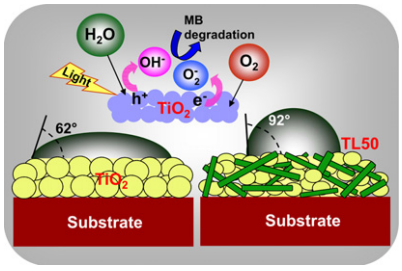

Multifunctional TiO_2–$LaPO_4$ composite stabilizes anatase phase with enhanced photocatalytic activity, and moderately higher hydrophobicity is a promising material for self-cleaning application.

Flux growth of a new cobalt–zinc–tin ternary phase $Co_{7+x}Zn_{3-x}Sn_8$ and its relationship to CoSn
Patricia C. Reynolds, Milorad Stojanovic and Susan E. Latturner
page 1875

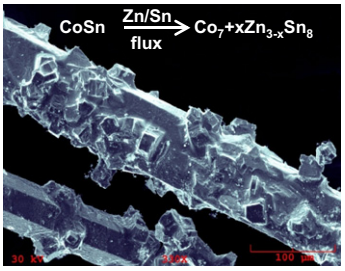

$Co_{7+x}Zn_{3-x}Sn_8$ forms from the reaction of cobalt in zinc/tin eutectic flux; it exhibits a *Cmcm* subcell or *Pnma* supercell depending on reactant stoichiometry.

Solid solubility of $Yb_2Si_2O_7$ in β-, γ- and δ-$Y_2Si_2O_7$
A.J. Fernández-Carrión, M.D. Alba, A. Escudero and A.I. Becerro
page 1882

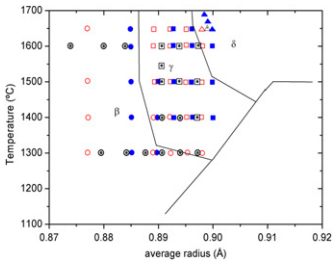

Polymorphism, as a function of average radii, in the systems $Yb_2Si_2O_7$–$Y_2Si_2O_7$ (dotted symbols), $Lu_2Si_2O_7$–$Y_2Si_2O_7$ (solid symbols) and $Sc_2Si_2O_7$–$Y_2Si_2O_7$ (open symbols) compared to phase boundaries of Felsche for pure rare earth disilicates. Circles: β-$RE_2Si_2O_7$. Squares: γ-$RE_2Si_2O_7$. Triangles: δ-$RE_2Si_2O_7$.

NdHO, a novel oxyhydride
Marius Widerøe, Helmer Fjellvåg, Truls Norby, Finn Willy Poulsen and Rolf Willestofte Berg
page 1890

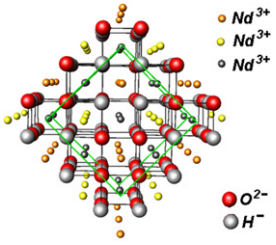

View of the NdHO structure.

Neutron powder diffraction, and solid-state deuterium NMR analyses of Yb_2RuD_6 and spectroscopic vibrational analysis of Yb_2RuD_6 and Yb_2RuH_6
Ralph O. Moyer Jr., Denis F.R. Gilson and Brian H. Toby
page 1895

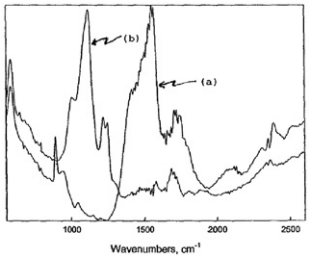

Using PAIR (see figure above) and FTIR data spectroscopic vibrational assignments are reported for (a) Yb_2RuH_6 and (b) Yb_2RuD_6. In addition, neutron powder diffraction structural elucidation data and deuterium NMR data are reported for Yb_2RuD_6.

Continued

Rapid Communication

Preparation of a new pyrochlore-type compound $Na_{0.32}Bi_{1.68}Ti_2O_{6.46}(OH)_{0.44}$ by hydrothermal reaction
Qiang Dong, Hong Jiang, Nobuhiro Kumada, Yoshinori Yonesaki, Takahiro Takei and Nobukazu Kinomura
page 1899

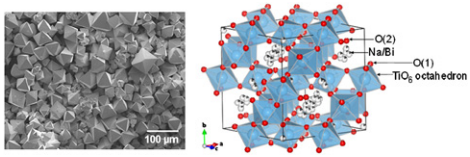

SEM image and schematic representation of the structure of $Na_{0.32}Bi_{1.68}Ti_2O_{6.46}$ $(OH)_{0.44}$.